Quantifying altimetric and volumetric changes of the Belvedere Glacier (2009–2023) using Pleiades and Pleiades Neo data

Francesco Ioli[1,2], Luca Cerina[2], Alberto Cina[3], Livio Pinto[2*]

[1] Research Institute for Geo-hydrological Protection (IRPI), Italian National Research Council, Turin, Italy – francescoioli@cnr.it
[2] Politecnico di Milano, Dept. of Civil and Environmental Engineering (DICA), Milan, Italy – livio.pinto@polimi.it; luca1.cerina@mail.polimi.it
[3] Department of Environment, Land, and Infrastructure Engineering (DIATI), Politecnico di Torino, Turin, Italy – alberto.cina@polito.it,

Keywords: VHR satellite photogrammetry, Pleiades, glacier monitoring, debris flow, hydrogeological risk.

Abstract

The study presents a detailed photogrammetric analysis of the evolution of the Belvedere Glacier over the periods 2009–2017 and 2017–2023, with particular focus on the impact of the debris flow triggered by the flood event of August 27, 2023. High-resolution Pléiades and Pléiades Neo satellite imagery was used to generate point clouds and Digital Elevation Models, enabling the quantification of altimetric and volumetric changes and a detailed assessment of the morphological modifications caused by the debris flow. The results show a recent significant glacier retreat, with an average annual volume loss of 2.3×10^6 m³/year between 2009 and 2017, increasing to 2.7×10^6 m³/year between 2017 and 2023. The 2023 debris flow produced marked morphological changes, including the formation of two accumulation zones on the western tongue and the development of two erosional channels approximately 4–5 meters deep. These channels resulted from the new course of the Castelfranco Stream, which incised directly into the glacier surface. Overall, the findings confirm trends reported in previous studies on the Belvedere Glacier and other Alpine glaciers, highlighting the importance and advantages of satellite-based monitoring for assessing the impacts of climate change and extreme events on glacier dynamics.

1. Introduction

Glaciers sensitivity to temperature fluctuations makes them powerful indicators of global climate change (Bojinski et al., 2014). Recent community assessments indicate that glaciers worldwide lost approximately 273 ± 16 Gton in mass annually from 2000 to 2023, with the rate of mass loss increasing by 36 ± 10% in the second half of the considered period (The GlaMBIE Team, 2025). Alpine glaciers in temperate zones are particularly susceptible to these rising temperatures with a mass change of -38.7% based on the glacier mass in 2000, compared to a global average mass loss of -5.4% (The GlaMBIE Team, 2025).
This rapid melting and retreat affect the local economy (Beniston et al., 2018), including freshwater supply, hydroelectric production (Barnett et al., 2005), and tourist activities. Furtermore, it leads to an increasing geohazard risk (Haeberli and Whiteman, 2015), with processes such as ice breakoffs, outbursts, and debris flows that threaten nearby infrastructure and populations (Deline et al., 2015). Among natural processes affecting high mountain environments, debris flows are one of the most dangerous (Tiranti et al., 2018). In debris flows, sediments can be easily mobilised by heavy precipitation, snowmelt or glacial lake outbursts (Chiarle et al., 2007; Yu et al., 2021).
Climate change is altering the frequency and magnitude of debris flows, acting both on meteorological forcing and sediment availability (Yu et al., 2021): glacier mass loss increases the instability of rock walls and glacier moraines through debuttressing. This results in a larger volume of loose sediments, while the increased ratio of rainfall to snowfall and glacier melt affects sediment mobilisation.
In this context, up-to-date accurate information plays a crucial role in glacier-related hazard monitoring. Photogrammetry and Structure-from-Motion/Multi-view Stereo (SfM/MVS) techniques can be effectively employed to remotely derive 3D data of remote and hazardous mountain areas, aiding in assessing and managing hydrogeological risks (Westoby et al., 2012). These methods provide geometrically accurate data useful to quantify morphological changes after hazardous events, such as mass movements or debris flows (Notti et al., 2021).
Monitoring these changes requires an integrated approach across different spatial and temporal scales. In the past decade, Uncrewed Aerial Vehicles (UAVs) have emerged as flexible, cost-effective tools for small to mid-scale 3D mapping, capable of acquiring data with centimeter-level spatial resolution, making them ideal for producing accurate orthophotos and Digital Elevation Models (DEMs) of regions affected by hydrogeological hazards (Ioli et al., 2021). However, they are limited by the need for intensive in situ manpower and significant altitude constraints. While effective for monitoring the lower glacier surface, UAVs are often unable to reach the steep upper accumulation areas where critical rock and ice avalanches originate.
At a mid-level scale, aerial surveys utilizing metric cameras provide decimetric resolution over larger areas (Macelloni et al., 2022). While historical aerial imagery is invaluable for long-term reconstructions (De Gaetani et al., 2021), modern aerial campaigns remain expensive and require complex organizational efforts for flight planning.
Recent advancements in Very High Resolution (VHR) satellite constellations like Pléiades and Pléiades Neo have offered broad-scale optical and multi-spectral imagery with resolutions as fine as 30 cm and stereoscopic capabilities, enabling detailed DSMs generation by SfM and quantification of these rapid morphological and volumetric changes (Giulio Tonolo, 2020; Macelloni et al., 2022). While VHR satellite imagery provides an invaluable overview of larger areas with no maximum altitude constraints, satellite imagery is usually expansive, especially for tasking acquisitions, and lack of long-term time series of images.

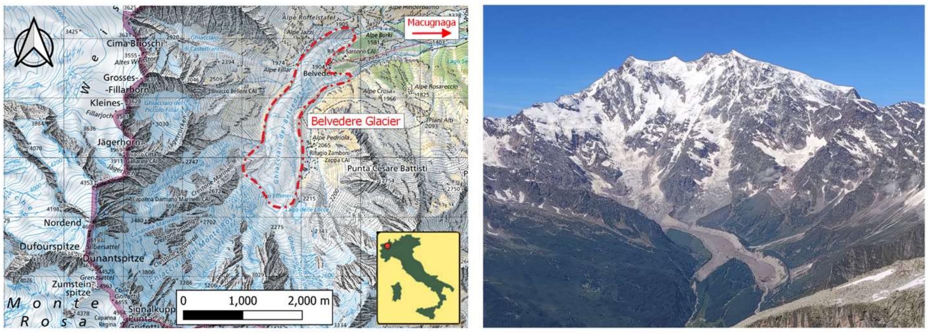

(a) (b)

Figure 1. (a) Location of the Belvedere Glacier (Italian Alps); and (b) view of the Belvedere and the overhanging Monte Rosa east face (basemap: Swisstopo - www.geo.admin.ch)

The goal of this study is to address these gaps by: (i) assessing the potential of VHR satellite stereo pairs for quantifying altimetric and volumetric changes across the entire Belvedere Glacier using modern SfM/MVS techniques. (ii) evaluating long-term elevation changes by combining archive stereo images (Pléiades) with tasked imagery and integrating them with aerial datasets to reconstruct the glacier's evolution between 2009 and 2023 (iii) experimenting with tasked acquisitions of Pléiades Neo data to evaluate the post-event impact of the August 27, 2023 debris flow. Furthermore, the challenges of tasked acquisitions, specifically how the acquisition viewing angle in steep, complex terrains can impact the precision of resulting Digital Elevation Models are finally discussed.

2. The Belvedere Glacier

The Belvedere Glacier is a debris covered valley glacier located on the east side of the Monte Rosa Massif (Italian Alps), within the municipality of Macugnaga (N 45°58′ E 7° 55′) (Fig. 1a). It extends between approximately 2,250 m and 1,800 m above sea level, spanning roughly 3 km in length and covering a current area of about 1.8 km². It is primarily fed by steep tributary glaciers, including the overlying hanging glaciers of Monte Rosa and Signal (Fig. 1b). The Nordend and Northern Locce, now detached from the Belvedere Glacier's main flow, are still contributing with frequent ice and snow avalanches.

Long-term analysis from 1977 to 2023 reveals a net loss of 54.28 × 10^6 m³ of ice volume (De Gaetani et al., 2021). Notably, recent sub-seasonal monitoring has documented the severe impact of the exceptionally hot and dry summer of 2022, which resulted in a peak volume loss of 4.90 × 10^6 m³ during the 2022–2023 period (Ioli et al., 2024a). During the 2022 season alone, the glacier snout experienced a frontal retreat of 17.8 m (Ioli, 2024c).

Over the last century, the basin has been a hotspot for significant geohazards (Kropáček et al., 2024), displaying a pronounced morphological dynamism driven by both climate change and the interaction of gravitational and hydrological processes. Notably, the unique surge event of 2001–2002 involved an accelerated ice flow that increased surface velocities up to 200 m/y. This surge created a topographic depression that led to the formation of Lago Effimero, a supraglacial lake that reached a volume of 3 million m³ and a depth of 57 m. The lake posed a severe flood risk to the village of Macugnaga before being managed by Civil Protection through emergency pumping (Kääb et al., 2005). The basin frequently experiences mass movements triggered by rapid deglaciation and permafrost degradation. Significant events include a massive 2005 ice avalanche (1.1 million m³) detaching from the Imseng channel area (Tamburini et al., 2013), a rock avalanche (~0.3 million m³) occurred in 2005 from the uppermost part of the Monte Rosa east face, and recurrent events from the Punta Tre Amici in 2010 (~0.1 million m³) and 2015 (0.2 million m³) (Chiarlie et al., 2016, Kropáček et al., 2024) a large ice avalanche (~0.35 million m³) in December 2024.

The steep Castelfranco gully, located on the orographic left side of the western tongue, between the Tyndall and Tuckett peaks, represents one of the most vulnerable sectors of the entire glacial system (Fig. 2). Here, the Castelfranco stream, which originates at elevations above 3,000 m a.s.l. has progressively altered its course since the mid-20th century, shifting from a path outside the lateral moraine to a route that is partly subglacial and partly supraglacial across the glacier snout. A particularly significant event occurred on September 7, 2008, when a flood triggered a debris flow that mobilized material along the gullies, channeling it to the lateral moraine with an estimated volume of the accumulated material of several thousand cubic meters. The vulnerability of this area was highlighted again by the event of August 27, 2023, which triggered a debris flow significantly larger than that of 2008, delivering approximately 200,000 m³ of sediment onto the glacier. The event led to the formation of new debris accumulations on the glacier surface and to a reorganization of the supraglacial drainage network, with the progressive incision of channels along the glacier snout (Fig 2). The morphological characteristics of the Castefranco gully, with steep slopes, abundant unconsolidated debris, and the contribution of rockfalls from the upper headwalls, represent predisposing factors for the reactivation of similar phenomena.

Figure 2. View of the Castelfranco gully and the breach along the Belvedere Glacier moraine opened by the flood of August 27, 2023 (red ellipse).

Overall, the Belvedere Glacier represents an emblematic case study for the integrated analysis of glacial dynamics and slope geomorphological instability in Alpine environments. Here, processes of glacier mass loss interact with debris flows and hydrographic reorganization, amplifying local hydrogeological risk.

https://doi.org/10.5194/isprs-archives-XLIX-B2-2026-429-2026

3. Datasets

The multi-temporal analysis of the evolution of the Belvedere Glacier is based on the integration of heterogeneous datasets acquired from different platforms and with varying spatial resolutions to ensure temporal continuity and adequate geometric accuracy. The reference model consists of a 2009 aerial photogrammetric DEM derived from an aerial survey (DMC camera, f = 120 mm) with a Ground Sampling Distance (GSD) of 40 cm, which was used as the benchmark for subsequent analysis (De Gaetani et al., 2021). For the intermediate period, a Pléiades satellite stereo pair acquired on August 15, 2017, was used, with a nominal GSD of 50 cm (panchromatic band, pansharpened). The stereo pair is shown in Fig. 3, while Tab. 1 presents its geometric characteristics, including viewing angles and convergence parameter. For the most recent epoch, a Pléiades Neo stereo pair acquired on October 17, 2023 (Fig. 4) was used, with a ground resolution of 30 cm, enabling a very high-resolution three-dimensional reconstruction of the glacier and the surrounding areas. The acquisition configuration and geometric setup of the scene are reported in Tab. 1. To complement the satellite data, a UAV survey was conducted on July 25, 2023 (DJI Matrice 300 equipped with a DJI P1 camera, f=35mm), before the debris flow event of August 27, 2023, during the Politecnico di Milano Summer School *Design and Implementation of Topographic Surveys for Territorial Monitoring in Mountain Environments* (Gaspari et al., 2025). This survey, characterized by high spatial resolution and centimetric accuracy, provided a pre-event three-dimensional model, which was essential for isolating and quantifying the morphological effects induced by the debris flow through multi-temporal comparisons.

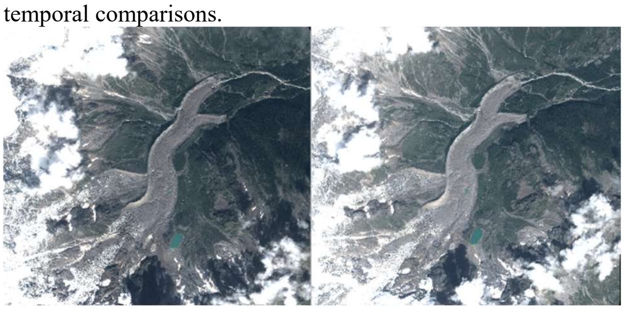

Figure 3. Stereo pair acquired by the Pléiades constellation on August 15, 2017

Figure 4. Stereo pair acquired by the Pléiades Neo constellation on October 17, 2023.

Table 1. Acquisition parameters of the Pléiades and Pléiades Neo imagery used in this study.

Acquisition Date	Incidence Angles [°]		Conv. angle [°]	B/H rat.
	Along track	Across track		
15/08/2017	15.88	9.98	27.01	0.48
15/08/2017	-11.11	16.01		
17/10/2023	-6.50	-47.50	15.88	0.28
17/10/2023	-26.60	-43.80		

The integrated dataset therefore covers the 2009–2023-time span at different levels of detail, ensuring both robustness in long-term volumetric comparisons and a high capacity for analyzing short-term morphological changes, particularly in relation to the extreme event of 2023.

4. Metodology

The multi-temporal three-dimensional reconstruction of the Belvedere Glacier was carried out using an integrated photogrammetric approach based on VHR satellite stereo pairs, UAV surveys, and a historical aerial photogrammetric model.
The entire workflow was structured into the following main phases: image pre-processing, photogrammetric orientation, DEM generation, validation, and DEM of Difference (DoD) analysis.

4.1 Satellite Image Pre-processing

The Pléiades (2017) and Pléiades Neo (2023) stereo images were first processed using a pansharpening routine to generate RGB products with a Ground Sample Distance (GSD) of 50 cm and 30 cm, respectively. This operation maximized spatial detail—essential for identifying homologous points in steep, debris-covered terrain—while preserving the radiometric information required for accurate 3D reconstruction. To inject the high-frequency spatial information of the panchromatic (PAN) band into the lower-resolution multispectral (MS) bands, the images were pansharpened using the Weighted Brovey transform (Pohl and Van Genderen, 1998) already implemented in the GDAL library.
The images were then imported into Agisoft Metashape, where the initial camera orientation and geometric model were established using the Rational Polynomial Coefficients (RPCs). These coefficients were automatically loaded by the software from the vendor-provided metadata files in DIM format, which provide the necessary mathematical parameters to relate image coordinates to ground coordinates.

4.2 Images orientation and Bundle Block Adjustment

To ensure multi-temporal consistency, a Bundle Block Adjustment (BBA) was performed to optimize the initial RPC-based orientation of each image block. Ground Control Points (GCPs) and Check Points (CPs) were derived photogrammetrically from the 2009 digital aerial photogrammetric model, thoroughly described in De Gaetani et al. (2020). These points correspond to stable natural features (e.g., distinctively shaped rocks) and artificial structures (e.g., building corners) that remained unchanged over time and could be reliably identified across the 2009 aerial imagery, the Pléiades, and the Pléiades Neo acquisitions. Orientation accuracy was validated using independent CPs (Figs. 5–6).

4.3 Point Clouds and DEM

Starting from the optimized image orientation, depth maps were generated using Agisoft Metasahpe dense stereo matching algorithms and subsequently converted into a dense point cloud. The point clouds were rasterized to produce DEMs with final resolutions of 1 m (2017) and 0.5 m (2023), which were then resampled to a common resolution of 1 m to ensure multi-temporal comparability.
For the analysis of the August 27, 2023 event, a UAV survey conducted on July 25, 2023 (pre-event), characterized by centimetric accuracy, was integrated (Ioli et al., 2024b). The

comparison between the UAV model (pre-debris flow) and the Pléiades Neo satellite model (post-debris flow) made it possible to isolate the morphological changes induced by the extreme event.

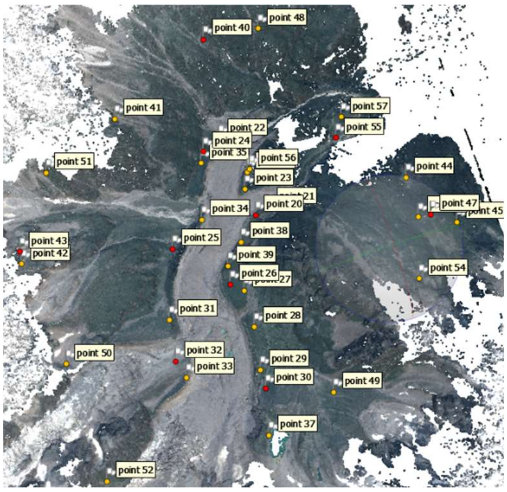

Figure 5. GCPs (in orange) and CPs (in red), 2017 model

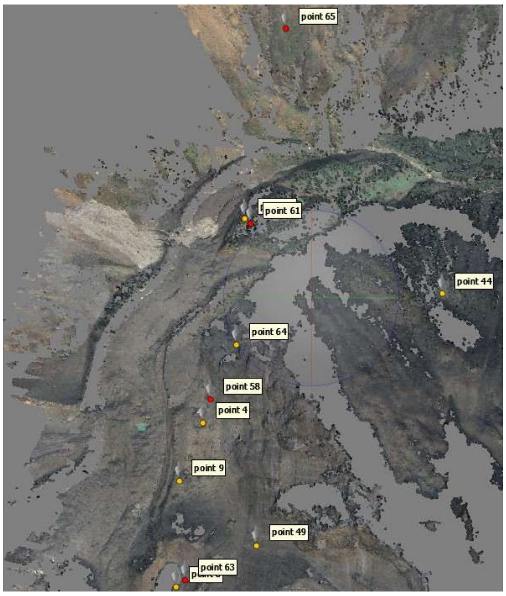

Figure 6. GCPs (in orange) and CPs (in red), 2023 model

4.4 Volumetric change and uncertainty estimation

Glacier surface elevation (Δh) changes between 2017 and 2023 were calculated by DoD. Total volumetric change (ΔV) was derived by summing the elevation differences across the glacier area at a processed resolution of 1 m.

The uncertainty of the elevation changes was estimated following the framework via the open source Python libraries *xdem* and *geoutils* (Hugonnet et al., 2022). This approach properly accounts for both heteroscedasticity (spatially variable errors) and spatial autocorrelation, which are often overlooked for glacial volumetric change estimation. The computational workflow consisted of three main steps:

1. Heteroscedasticity Modelling: elevation errors are often correlated with terrain geometry. We assessed elevation differences on stable off-glacier terrain, defined by masking out glaciers (using Randolph Glacier Inventory 7.0 outlines) and known unstable sectors like debris flows. We mapped the spatially variable error, $\sigma_{\Delta h}$, by modelling the Normalized Median Absolute Deviation (NMAD) of the differences against terrain slope and maximum curvature.
2. Spatial Autocorrelation: to decouple the spatial correlation patterns from the terrain-related heteroscedasticity, we standardized the residuals into z-scores ($z = \Delta h/\sigma_{\Delta h}$). The spatial correlation of these standardized errors was quantified by averaging 15 empirical variograms (subsampled at 5,000 points per variogram) over the stable terrain. This step models the correlation function (i.e., the degree of spatial dependence between any two pixels and separated by a given distance) and identifies the correlation length (i.e., the distance beyond which elevation errors become independent).
3. Error Propagation: The uncertainty was propagated explicitly to the glacier area. Rather than assuming pixels are independent, the spatial correlation function was integrated over the glacier geometry to correctly scale the variance. The variance of the mean elevation changes over the glacier, $\sigma^2_{\overline{\Delta h}}$, was approximated by double-summing the covariance matrix across valid glacier pixels (i.e., pixels with non-null elevation difference within the Belvedere Glacier area) (Eq. 1):

$$\sigma^2_{\overline{\Delta h}} = \frac{1}{N^2} \sum_{i \in A} \sum_{j \in A} \sigma_i \, \sigma_j c_{i,j} \quad (1)$$

Where N is the number of valid pixels in the glacier area A, σ_i and σ_j are the predicted heteroscedastic errors at locations i and j, and $c_{i,j}$ is their spatial correlation derived from the variogram model. This exact integration mathematically yields the effective number of independent observations (N_{eff}) that replaces the number of valid pixels N, and standard error of the average elevation change ($SE_{\overline{\Delta h}}$).

Finally, the uncertainty of the total volumetric change was calculated by multiplying the standard error by the glacier area. Final uncertainties are reported at a 95% confidence interval ($1.96 \times SE_{\overline{\Delta V}}$) (Hugonnet et al., 2022).

5. Results

5.1 DEM reconstruction and error assessment

The photogrammetric processing of the satellite stereo pairs allowed for the generation of high-resolution Digital Elevation Models (DEMs) for both the 2017 and 2023 epochs (Fig. 7). The 2017 reconstruction, derived from Pléiades 1A/1B imagery, provided a nearly complete topographical model of the study area, successfully capturing the steep slopes of the Belvedere basin. However, the upper ridges of the Monte Rosa massif (located in the left and bottom sectors of Fig. 4) were obscured by cloud cover during acquisition. This resulted in localized random noise in the raw output, which was manually masked and

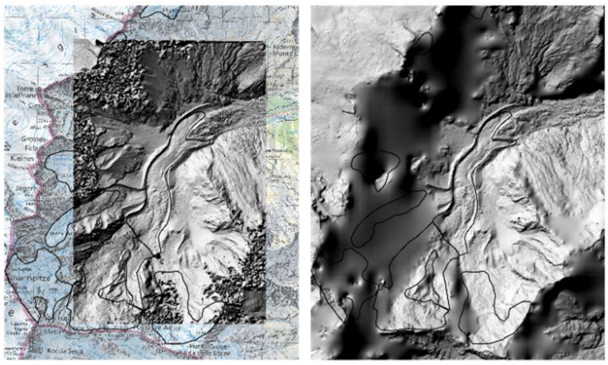

(a) (b)

Figure 7. Hillshaded DEM obtained from (a) 2017 Plaides 1A/1B imagery; (b) 2023 Pléiades Neo imagery.

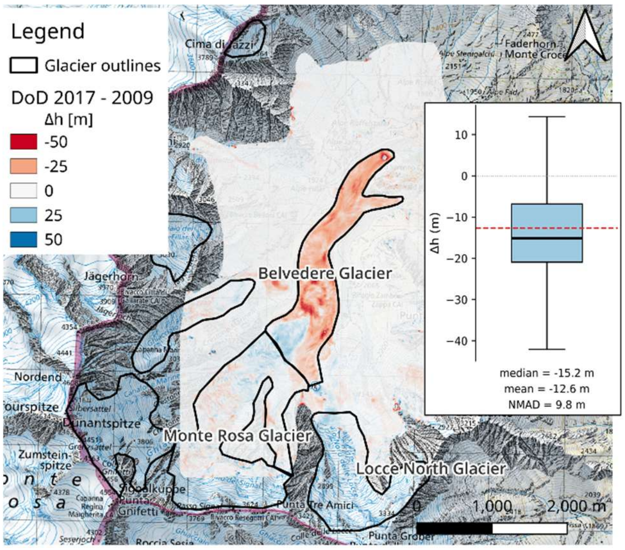

Figure 8. Spatial distribution of surface elevation changes (DoD) of the Belvedere Glacier between 2009 and 2017. The map displays pixel-wise height differences. The boxplot summarizes the statistical distribution of Δh within the glacier area

removed to ensure the integrity of the final geomorphological analysis.

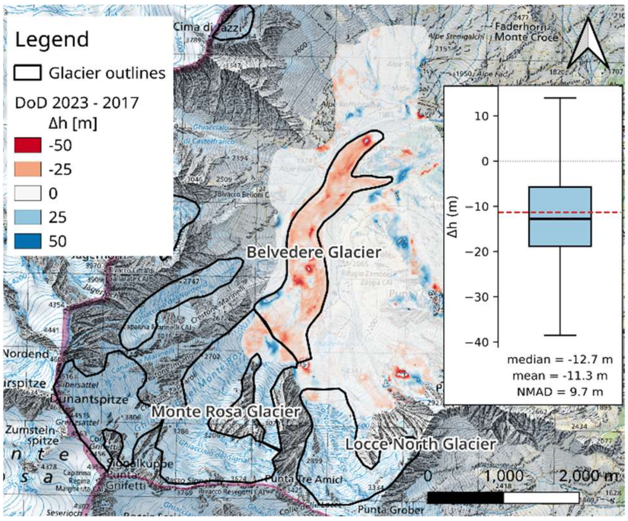

Figure 9. Spatial distribution of surface elevation changes (DoD) of the Belvedere Glacier between 2017 and 2023. The map displays pixel-wise height. The boxplot summarizes the statistical distribution of Δh within the glacier area.

In contrast, the 2023 reconstruction using Pléiades Neo imagery proved more technically challenging due to suboptimal acquisition geometry (Table 1). The 2023 stereo pair was characterized by very low incidence angles and a viewpoint positioned directly behind the steep Monte Rosa East Face. These factors, combined with a low convergence angle (15.88°) and a reduced B/H ratio of 0.28, created a poor photogrammetric configuration compared to the 2017 dataset (B/H of 0.48), with large extrapolated and unreliable areas, which were excluded.
The quality of the photogrammetric reconstructions was evaluated through a dual-stage process involving both independent check points and analysis of stable terrain. Regarding point-based accuracy, the evaluation at individual CPs (10 in the 2017 model and 4 in the 2023 one), yielded a Root Square Mean Error (RMSE) of 0.39 m for the 2017 model and 0.54 m for the 2023 model. These values remain consistent with the image GSD and the inherent uncertainty of the GCPs extracted from the 2009 aerial model.
To validate the reliability of elevation change measurements across the entire study area, residuals were calculated over stable, non-glaciated ground across multiple temporal comparisons, using the 2009 DEM as reference.
For the 2017 DEM, vertical residuals on stable terrain—calculated as the median of the differences between the satellite and the 2009 reference models—yielded an NMAD of 1.06 m and a median vertical bias of 0.02 m. In contrast, the 2023 model showed higher uncertainty, with an NMAD of 2.61 m and a bias of 0.20 m. This performance gap is primarily attributed to the sub-optimal acquisition geometry of the 2023 stereo pair; a comprehensive analysis of these error sources is provided in Sec.6.

5.2 Elevation and volumetric changes (2009–2023)

The analysis of elevation changes by DoD enabled a robust quantification of glacier volumetric losses of the Belvedere Glacier over the two investigated periods: 2009–2017 and 2017–2023.
During 2009–2017, the results indicate a widespread surface lowering of the Belvedere Glacier, with a mean elevation change (Δh) of −12.64 ± 0.35 m (95% confidence interval), where the standard deviation of the mean elevation change was computed using the methodology described in Sec. 4.4. The spatial distribution of these changes reveals that the most intense thinning is concentrated in the terminal sectors of the north-western lobe, where local lowering values exceed 40 m and reach peaks larger than 50 m near the glacier snout (Fig. 8). The integrated volumetric balance for this 8-year period confirms a total ice volume loss of 18.4 ± 0.26 × 10^6 m^3, corresponding to an average annual ablation rate of 2.3 ± 0.03 × 10^6 m^3/year.
In the second period (2017–2023), the glacier experienced a significant acceleration in mass loss. The mean surface lowering reached −11.33 ± 0.55 m (95% CI) over 6 years (Fig. 9). This period is characterized by a nearly two-fold increase in the rate of deglaciation compared to the previous interval, resulting in a total volume loss of 16.5 ± 0.80 × 10^6 m^3. The average annual ablation rate resulted in 2.7 ± 0.05 × 10^6 m^3/year. This acceleration aligns with regional Alpine trends and can be attributed to exceptionally hot and dry summers, particularly in 2022, which caused peak ablation across the entire glacier surface (Ioli, 2024c).

5.3 Cross-sections and morphodynamic analysis

The analysis of longitudinal and transverse cross-sections (Fig. 10) allows for the division of the Belvedere Glacier into four distinct morphodynamic units, each exhibiting a unique response to climatic forcing over the study period.

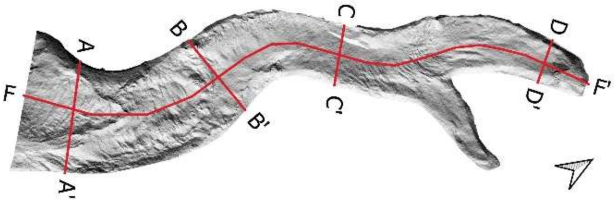

Figure 10. Location of the cross-sections profiles.

This contribution has been peer-reviewed.
https://doi.org/10.5194/isprs-archives-XLIX-B2-2026-429-2026 |

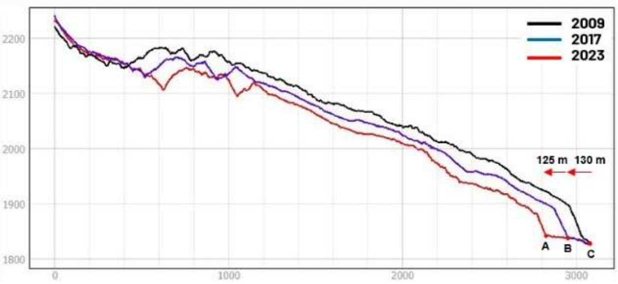

Figure 11. Longitudinal profiles along section FF' along the glacier flow line.

1. Upper accumulation zone. The longitudinal profile FF' (Fig. 11) and transverse section AA' (Fig. 12) characterize the highest reaches of the glacier. In this sector, a phase of positive mass balance was documented during the 2009–2017 period, with elevation gains up to 12 m. Although this area remained above the equilibrium line in terms of volumetric balance until 2017, the 2017–2023 interval marked a reversal of this trend. Recent data shows a general surface lowering between 2 and 9 m, signaling that the accumulation zone is no longer sufficiently compensated by winter precipitation to offset rising summer ablation.

2. Upper ablation zone. Located immediately downstream of the accumulation area, this sector is characterized by a strongly non-linear evolution and significant morphological reorganization (Profile BB', Fig. 13). This zone, which recurrently hosts supraglacial lakes and is subject to intense crevassing, has transitioned into a highly erosional state. The thinning in this area has accelerated dramatically in the second period, with localized depressions reaching values of up to 50 m

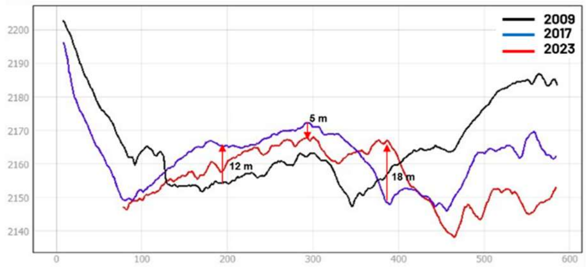

Figure 12. Transversal section along the profile AA' in the upper accumulation zone.

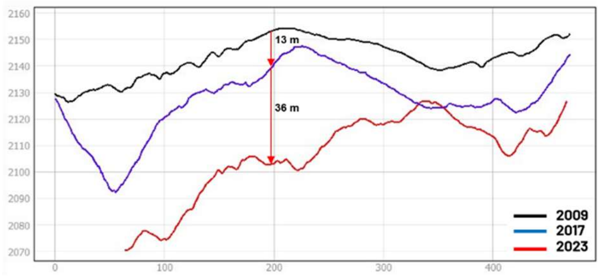

Figure 13. Transversal section along the profile BB' in the upper ablation zone

3. Lower ablation zone (main flow). The central body of the glacier, represented by transverse cross-section CC' (Fig. 14), shows a more stable and linear response to climatic forcing. Unlike the upper sections, this area exhibits a relatively homogeneous thickness loss of approximately 20 m in both the 2009–2017 and 2017–2023 periods. This uniform thinning across the glacier surface indicates a steady negative mass balance.

4. Glacier snouts: The terminal sector, particularly the northwestern lobe, represents the most critical area of regression. The longitudinal profile FF' (Fig. 11) documents a total retreat of approximately 255 m over 14 years. The retreat was relatively steady, with 130 m lost between 2009 and 2017 (avg. 16.3 m/year) and 125 m lost in the shorter 6-year span between 2017 and 2023 (avg. 20.8 m/year). Cross-sections DD' (Fig. 15) further highlights the intensity of the collapse at the terminus, with vertical surface lowering reaching 57–60 m.

Overall, the sectional analysis confirms a differentiated but increasingly synchronized behavior along the glacier axis: while the central flow thins steadily, the accumulation head is shrinking, and the terminal snouts are retreating at an accelerating pace.

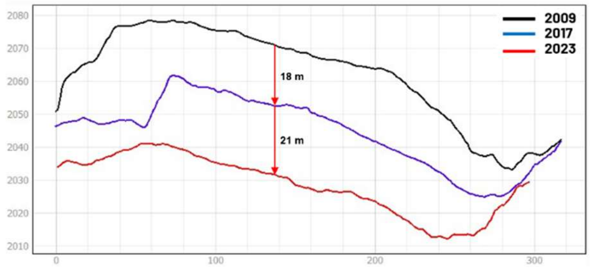

Figure 14. Transversal section along the profile CC' in the lower ablation zone

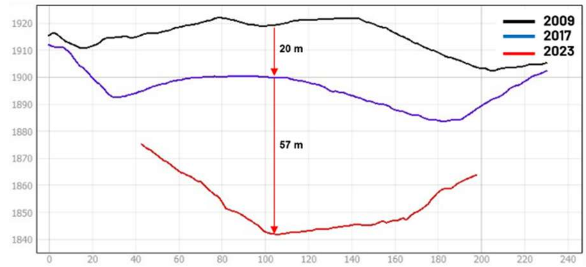

Figure 15. Transversal section along the profile DD' in the northwestern snout.

5.4 Analysis of the August 27, 2023 debris flow event

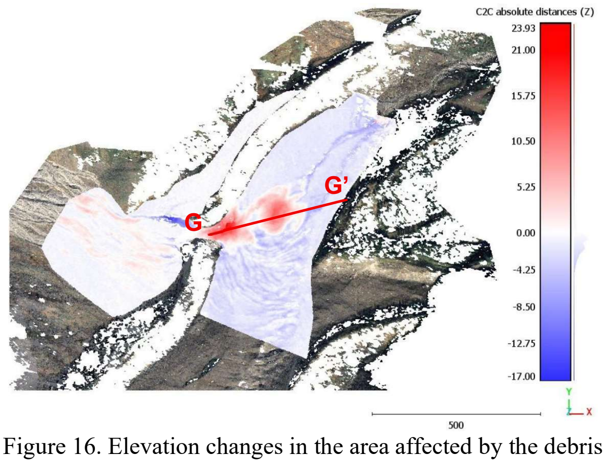

Figure 16. Elevation changes in the area affected by the debris flow on August 27, 2023. Colors represent differences between the post- and pre-event photogrammetric point clouds along the vertical direction. Values are expressed in meters.

To quantify the morphological impact of the August 27, 2023 flood, we compared the pre-event UAV survey (July 25, 2023) with the post-event Pléiades Neo satellite model (October 17, 2023). The analysis focused on the debris flow's trajectory from the Castelfranco slope onto the glacier's western tongue. The event resulted in two primary debris accumulation zones on the

glacier surface (Fig. 16), with a total estimated volume of ~180,000 m³. The largest deposit is located where the Castelfranco stream overtopped the left lateral moraine, while a second, more distal lobe reached the center of the tongue.
Analysis of cross-section GG' (Fig. 17) reveals significant geomorphological reorganization. Along the slope, the flow incised new channels up to 4–5 m deep directly into the glacier ice. This incision reflects a major shift in supraglacial drainage following the obstruction of the former endo-glacial pathway.
Volumetric budgets for the tongue area indicate a massive net gain of ~180,000 m³ of debris, partially offset by ~33,000 m³ of localized ice erosion and thermal karst development. On the contributing slope, approximately 69,000 m³ of material was mobilized from the terminal sector of the Castelfranco channel.
Comparison with the 2017–2023 topographic trend suggests the 2023 event was the culmination of a multi-year sediment build-up in the upper catchment. Ultimately, the 2023 debris flow exceeded the magnitude of the 2008 event, underscoring the intensifying coupling between slope instability and rapid glacier thinning in high-alpine environments.

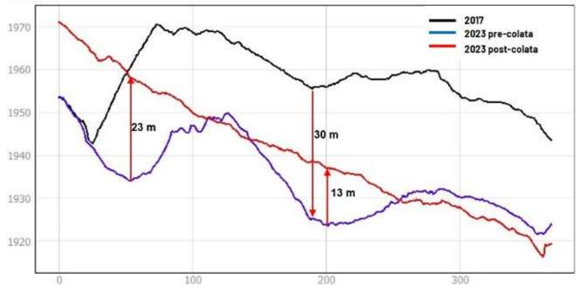

Figure 17. Elevation profiles extracted along the cross-section GG' located along the median axis of the debris accumulation deposit on top of the glacier terminal lobe.

6. Discussion

VHR satellite imagery proves to be a robust tool for quantifying altimetric and volumetric changes across the entire Belvedere Glacier. While the vertical accuracy (NMAD of 1.06–2.61 m) is approximately one order of magnitude lower than that achievable through UAV photogrammetry (typically sub-decimetric), it remains well within the threshold required for meaningful mass balance estimation. A primary advantage is the elimination of intensive in-situ surveys. By utilizing *virtual* GCPs extracted from prior datasets with comparable accuracy (e.g., another photogrammetric/LIDAR survey), it is possible to generate georeferenced 3D models with GSD-level precision, even when field access is restricted.
Furthermore, satellite platforms overcome a major limitation of UAVs by providing coverage of high-elevation accumulation zones. However, the extreme topography of the Monte Rosa east face remains a significant challenge; even with sub-meter resolution, the steepest rock and ice walls are prone to reconstruction artifacts or data gaps, as evidenced by the cloud-induced noise and geometric stretching in the upper ridges.
The use of tasked Pléiades Neo imagery allowed for a rapid post-event assessment of the August 2023 debris flow, proving that "on-demand" satellite photogrammetry is a viable alternative to aerial surveys for disaster response. Nevertheless, this study identifies critical constraints:
1. Geometric vulnerability. Tasked acquisitions are highly sensitive to the satellite's orbit and the vendor's queuing priorities. In the 2023 case, the acquisition geometry was sub-optimal (low B/H ratio and high incidence angles), leading to a significantly lower accuracy (NMAD 2.61 m) despite the superior 30 cm GSD of the Pléiades Neo sensor. This highlights that for steep, non-flat terrain, sensor resolution is secondary to acquisition geometry.
2. Operational constraints. High costs and variable archival availability remain significant barriers. Furthermore, the reliance on favourable meteorological conditions and the company's tasking queue can delay post-event acquisitions, potentially missing transient morphological features.

7. Conclusions

This study successfully reconstructed the surface evolution of the Belvedere Glacier between 2009 and 2023 by integrating multi-source photogrammetric data. The results confirm a dramatic acceleration in glacier mass loss, with the mean downwasting rate increasing nearly eightfold compared to the mid-20th century. The sectional analysis revealed a shifting dynamic where the accumulation zone is no longer capable of compensating for the accelerating retreat of the terminal snouts, which reached horizontal recession rates of over 20 m/year in the recent period. The experimentation with Pléiades Neo tasking demonstrated the potential for quantifying large-scale geomorphological impacts, such as the 180,000 m³ debris flow of August 2023. However, we conclude that the precision of such models is strictly governed by the acquisition viewing angles in complex terrains.
Future work should focus on optimizing the photogrammetric processing of satellite stereo pairs in steep terrain. This includes testing alternative open-source pipelines such as the NASA Ames Stereo Pipeline (Shean et al., 2016) and MICMAC (Rupnik et al., 2017), which offer specialized algorithms for satellite and topographic data. Particularly for challenging geometries like the 2023 Pléiades Neo dataset, the integration of deep-learning-based matching algorithms represents a promising frontier. State-of-the-art solutions for robust dense (Morelli et al., 2024), could significantly improve reconstruction completeness and accuracy where traditional Structure-from-Motion techniques struggle due to low convergence angles or high perspective distortion. Ultimately, as satellite constellations increase in temporal frequency, the potential for near-real-time monitoring of glacier kinematics and paraglacial hazards becomes a tangible goal for Alpine risk management.

Acknowledgements

The authors acknowledge the financial support of Fondazione Cariplo (project: MOHYCAM - Modified HYdrogeological hazards under complex ClimAte and environmental conditions: Monitoring activities and mitigation strategies -grant no. 2024-3388).

References

Barnett, T. P., Adam, J. C., Lettenmaier, D. P., 2005: Potential impacts of a warming climate on water availability in snow-dominated regions. *Nature*, 438, 303–309.

Beniston, M., Farinotti, D., Stoffel, M., et al., 2018: The European mountain cryosphere: a review of its current state, trends, and future challenges, *The Cryosphere*, 12, 759–794.

Bojinski, S., Verstraete, M., Peterson, T. C., Richter, C., Simmons, A., Zemp, M., 2014: The Concept of Essential Climate Variables in Support of Climate Research, Applications, and Policy. *Bull. Amer. Meteor. Soc.*, **95**, 1431–1443.

Chiarle, M., Iannotti, S., Mortara, G., Deline, P., 2007: Recent debris flow occurrences associated with glaciers in the Alps. *Global and Planetary Change*, 56, 123–136.

Chiarle, M., Mortara, G., Tamburini, A., Martelli, M., Sergio, G., Cat Berrò, S., 2016: Il crollo del 16-17 dicembre 2015 alla Punta Tre Amici (Macugnaga, Monte Rosa). *http://www. nimbus. it/ghiacciai/2016/160119_CrolloTreAmici.*

De Gaetani, C. I., Ioli, F., Pinto, L., 2021: Aerial and UAV images for photogrammetric analysis of belvedere glacier evolution in the period 1977–2019. *Remote Sensing*, *13*(18), 3787.

Deline, P., Gruber, S., Delaloye, R., Fischer, L., Geertsema, M., Giardino, M., Hasler, A., Kirkbride, M., Krautbletter, M., Magnin, F., McColl, S., Ravanel, L., Schoeneich, P., 2015: Ice loss and slope stability in high-mountain regions. *Snow and ice-related hazards, risks, and disasters* (pp. 521-561). Academic Press.

Gaspari, F., Barbieri, F., Fascia, R., Ioli, F., Pinto, L., Migliaccio, F., 2025: Strategies for Glacier Retreat Communication with 3D Geovisualization and Open Data Sharing. *ISPRS International Journal of Geo-Information*, 14(2), 75.

Giulio Tonolo, F., Cina, A., Manzino, A., Fronteddu, M., 2020: 3D glacier mapping by means of satellite stereo images: the belvedere glacier case study in the italian alps, *Int. Arch. Photogramm. Remote Sens. Spatial Inf. Sci.,* XLIII-B2-2020, 1073–1079.

Haeberli, W., Whiteman, C., 2015: Snow and Ice-Related Hazards, Risks, and Disasters: A General Framework. *Snow and ice-related hazards, risks, and disasters* 1–34 Academic Press.

Hugonnet, R., Brun, F., Berthier, E., Dehecq, A., Mannerfelt, E. S., Eckert, N., Farinotti, D., 2022: Uncertainty analysis of digital elevation models by spatial inference from stable terrain. *IEEE Journal of Selected Topics in Applied Earth Observations and Remote Sensing*, *15*, 6456-6472.

Ioli, F., Bianchi, A., Cina, A., De Michele, C., Maschio, P., Passoni, D., Pinto, L., 2021: Mid-Term Monitoring of Glacier's Variations with UAVs: The Example of the Belvedere Glacier. *Remote Sensing* 14, 28.

Ioli, F., Dematteis, N., Giordan, D., Nex, F., Pinto, L., 2024a: Deep Learning Low-cost Photogrammetry for 4D Short-term Glacier Dynamics Monitoring. *PFG – Journal of Photogrammetry, Remote Sensing and Geoinformation Science*. 92, 657–678.

Ioli, F., De Gaetani, C., Barbieri, F., Gaspari, F., Pinto, L., Rossi, L., 2024b: Belvedere Glacier long-term monitoring Open Data - Pointclouds, DEMs, Orthophotos (2.0) [Data set]. Zenodo. DOI: 10.5281/zenodo.7842347.

Ioli, F., 2024c: Multi-temporal and Multi-scale photogrammetry for Alpine Glacier Monitoring. Politecnico di Milano, PhD Thesis. https://hdl.handle.net/10589/224092.

Kääb, A., Huggel, C., Fischer, L., Guex, S., Paul, F., Roer, I., Salzmann, N., Schlaefli, S., Schmutz, K., Schneider, D., Strozzi, T., Weidmann, Y., 2005: Remote sensing of glacier-and permafrost-related hazards in high mountains: an overview. *Natural Hazards and Earth System Science*, 5(4), 527–554.

Kropáček, J., Mehrishi, P., Bollati, I. M., Brodský, L., Pelfini, M., Azzoni, R., Schmidt, S., Nüsser, M., Vilímek, V., 2024: Dynamics and related hazards of the Belvedere Glacier in the Italian Alps: a review. *AUC Geographica* 59(2), 163–183.

Macelloni, M. M., Corte, E., Ajmar, A., Cina, A., Giulio Tonolo, F., Maschio, P. F., Pisoni, I. N., 2022: Multi-platform, Multi-scale and Multi-temporal 4D Glacier Monitoring. The Rutor Glacier Case Study. In *Italian Conference on Geomatics and Geospatial Technologies* (pp. 392-404). Springer International Publishing.

Morelli, L., Ioli, F., Maiwald, F., Mazzacca, G., Menna, F., Remondino, F., 2024: Deep-image-matching: a toolbox for multiview image matching of complex scenarios. *Int. Arch. Photogramm. Remote Sens. Spatial Inf. Sci*., XLVIII-2/W4-2024, 309–316.

Notti, D., Giordan, D., Cina, A., Manzino, A., Maschio, P., Bendea, I. H., 2021: Debris flow and rockslide analysis with advanced photogrammetry techniques based on high-resolution RPAS data. Ponte Formazza case study (NW Alps). *Remote Sensing*, 13(9), 1797.

Pohl, C., Van Genderen, J. L., 1998: Multisensor image fusion in remote sensing: concepts, methods and applications. *International Journal of Remote Sensing*, 19(5), 823-854.

Rupnik, E., Daakir, M. & Pierrot Deseilligny, M., 2017: MicMac – a free, open-source solution for photogrammetry. *Open geospatial data, softw. stand.* 2, 14.

Shean, D. E., O. Alexandrov, Z. Moratto, B. E. Smith, I. R. Joughin, C. C. Porter, Morin, P. J., 2016: An automated, open-source pipeline for mass production of digital elevation models (DEMs) from very high-resolution commercial stereo satellite imagery. *ISPRS Journal of Photogrammetry and Remote Sensing*. 116.

Tamburini, A., Villa, F., Fischer, L., Hungr, O., Chiarle, M., Mortara, G., 2013: Slope Instabilities in High-Mountain Rock Walls. Recent Events on the Monte Rosa East Face (Macugnaga, NW Italy). *Landslide Science and Practice*. Springer

The GlaMBIE Team, 2025: Community estimate of global glacier mass changes from 2000 to 2023. *Nature.* 639, 382–388.

Tiranti, D., Crema, S., Cavalli, M., Deangeli, C., 2018: An Integrated Study to Evaluate Debris Flow Hazard in Alpine Environment. *Frontiers in Earth Science*, 6, 60.

Westoby, M. J., Brasington, J., Glasser, N. F., Hambrey, M. J., Reynolds, J. M., 2012: 'Structure-from-Motion' photogrammetry: A low-cost, effective tool for geoscience applications. *Geomorphology*, 179, 300-314.

Yu, G. A., Yao, W., Huang, H. Q., Liu, Z., 2021: Debris flows originating in the mountain cryosphere under a changing climate: A review. *Progress in Physical Geography: Earth and Environment*, 45(3), 339-374.